nature cell biology

Actin dynamics modulate mechanosensitive immobilization of E-cadherin at adherens junctions

W. Engl[1], B. Arasi[1], L. L. Yap[2], J. P. Thiery[1,2,3,5] and V. Viasnoff[1,4,5,6]

Mechanical stress is increasingly being shown to be a potent modulator of cell–cell junctional morphologies in developmental and homeostatic processes. Intercellular force sensing is thus expected to be an important regulator of cell signalling and tissue integrity. In particular, the interplay between myosin contractility, actin dynamics and E-cadherin recruitment largely remains to be uncovered. We devised a suspended cell doublet assay to quantitatively assess the correlation between myosin II activity and local E-cadherin recruitment. The single junction of the doublet exhibited a stereotypical morphology, with E-cadherin accumulating into clusters of varied concentrations at the rim of the circular contact. This local recruitment into clusters derived from the sequestration of E-cadherin through a myosin-II-driven modulation of actin turnover. We exemplify how the regulation of actin dynamics provides a mechanism for the mechanosensitive response of cell contacts.

E-cadherin (E-cad)-mediated intercellular adhesion and its associated regulatory processes play critical roles in morphogenesis, tissue repair[1–3], maintenance of tissue integrity, and cancer dissemination[4]. These mechanisms are studied at the levels of gene expression, protein trafficking and molecular signalling[5–7]. The interplay between tensile forces and adhesion of intercellular contacts is increasingly identified as a key regulatory mechanism in morphogenetic processes in embryos and within organs[8–11]. In particular, studies have reported myosin II-dependent E-cad recruitment[12,13] and spatial organization[14,15] at cell–cell contacts. In turn, polarization of the periodic flux of apical contraction can be induced by a heterogeneous distribution of cadherin[16]. E-cad organizes into puncta[17–20] with different dynamic properties depending on the cell type, maturation[17] and localization at the contact[21,22]. *Trans* and *cis* dimerization are sufficient to initiate cluster formation[4,23,24]. However, binding of the E-cad cytoplasmic domain to the cytoskeleton provides stability and directional motion to adhesive clusters[25]. Therefore, it seems that the actin structure plays an essential role in E-cad organization and adhesion strength[22,26]. Coupling between E-cad and cortical actin is a dynamic process mediated by a variety of proteins such as α-catenin, myosin VI, vinculin and EPLIN; the recruitment of these proteins endows mechanosensitivity to the cell–cell junction. Indeed, on stretching, a conformational change in α-catenin[27] leads to the recruitment of vinculin and subsequently actin, which strengthens the interaction between cadherins and the actin network. In *Drosophila melanogaster*, E-cad puncta were reported to interact with a highly stable pool of actin[28]. The stiffness of cadherin-coated substrates[29] and mechanical stimulation with cadherin-coated beads[30] also induce various levels of local recruitment of both actin and cadherin. Collectively, it raises questions on how adhesion strength is affected by the dynamic properties of actin, and how these properties depend on myosin II contractility. Here, we study the interplay between internally generated tensile forces, cortical actin dynamics and E-cad recruitment at cell–cell contacts.

RESULTS

E-cad forms clusters at the contact rim in an actin-anchoring–dependent manner

To investigate E-cad mechanosensitive regulation, we devised a cell doublet assay where cell junctions of reproducible morphologies form in the absence of extracellular matrix adhesion. The method consists of stacking a pair of suspended cells in a non-adhesive microwell, which is index-matched with the cell culture medium. It permits the fast, live, three-dimensional (3D) spinning-disc imaging of the intercellular contact in an *en face* geometry (Fig. 1a). Custom Matlab image analysis then corrects for all spontaneous residual rotations of the doublet (Supplementary Fig. 1a,b and Videos 1 and 2). Therefore, the recruitment dynamics of a GFP-tagged E-cad protein can be followed in real time from the onset of intercellular contact in the frame of reference of the junction. E-cad adhesion specificity was assured using

[1]Mechanobiology Institute, National University of Singapore, 5A Engineering Drive 1, Singapore 117411, Singapore. [2]Department of Biochemistry, Yong Loo Lin School of Medicine, National University of Singapore, 8 Medical Drive, Singapore 117596, Singapore. [3]Institute of Molecular Cell Biology, A*STAR, 61 Biopolis Drive, Singapore 138673, Singapore. [4]CNRS/ESPCI Paristech, 10 rue Vauquelin 75005 Paris, France. [5]Co-senior authors.
[6]Correspondence should be addressed to V.V. (e-mail: virgile.viasnoff@espci.fr)

Received 5 November 2013; accepted 24 April 2014; published online 25 May 2014; DOI: 10.1038/ncb2973

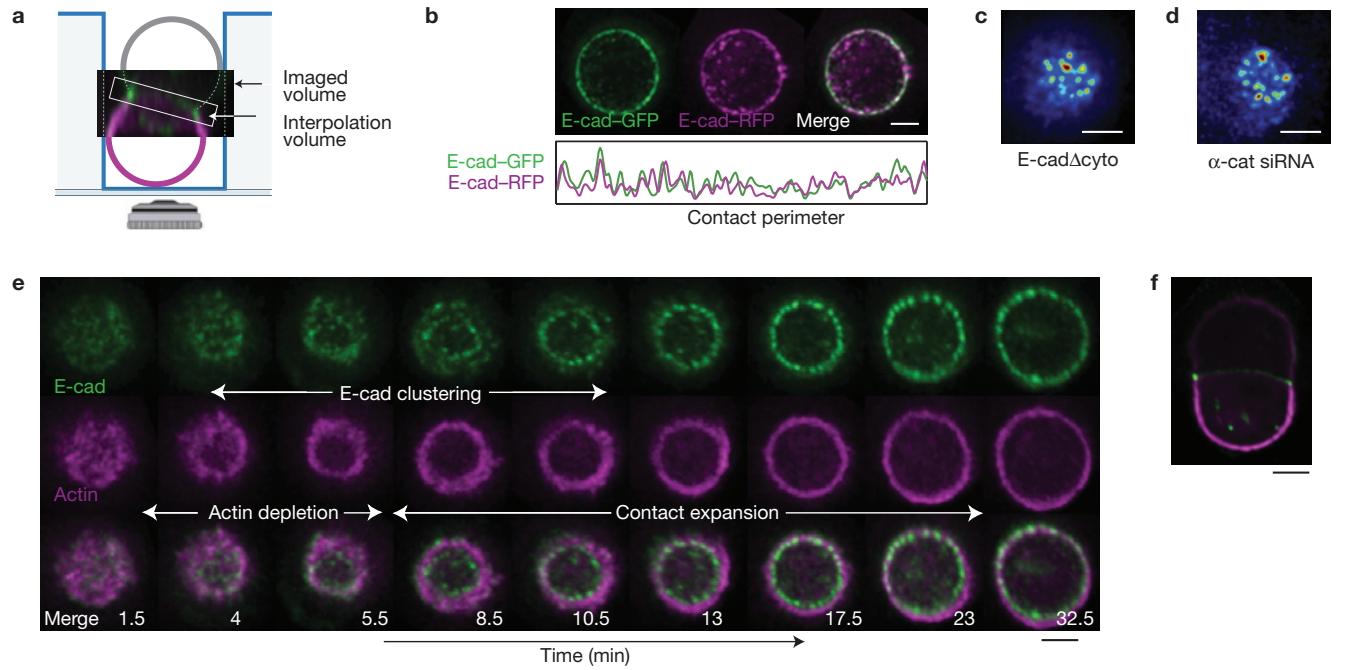

Figure 1 E-cad herin (E-cad) organizes into stable clusters at the contact rim in an actin anchoring-dependent manner. (**a**) Schematic side view of the cell doublet in the microwell. (**b**) Contact view of a hetero-doublet E-cad–GFP/E-cad–RFP (top). Profiles along the ring for E-cad–GFP and E-cad–RFP (bottom). (**c**) Contact view of an S180wt doublet expressing E-cad without a cytoplasmic domain. (**d**) Contact view of an S180 doublet with α-catenin knockdown. (**e**) Time-lapse sequence of cell–cell junction formation. (**f**) Equatorial plane of the doublet at steady state. Scale bars, 5 μm.

S180-E-cad–GFP, a murine sarcoma cell line (S180wt; refs 31,32) deprived of endogenous cadherin and stably transfected with E-cad–GFP. Over 1 h, we observed the radial growth of planar cell–cell contacts with a three- to sixfold accumulation of E-cad at the contact rim into distinctly spaced clusters (Fig. 1e). Throughout the contact area, cadherin presented a relatively homogeneous distribution, with few very mobile and transient clusters; the average density was close to that away from the junction in spite of the presence of the two contacting membranes (Supplementary Fig. 5c). Similar distributions were also observed in MDCK and embryonic stem cell doublets (Supplementary Fig. 1c), and in zebrafish epiblasts, as reported in ref. 26. Hetero-doublets of E-cad–GFP- and E-cad–RFP-expressing cells exhibited an enhanced cadherin co-localization in each puncta, which advocated for *trans* dimerization mainly at the contact edge (Fig. 1b) and poor co-localization over the contact surface. With our optical resolution, we could not decipher whether these regions of enhanced cadherin concentration were true molecular clusters or aggregates of nanoscopic clusters, as observed previously[33]. E-cad clusters were estimated to comprise around 100–300 molecules, based on the total number of cadherins in the cell (50,000–150,000) and on the local enrichment in the 0.4 μm^2 cluster area (Supplementary Fig. 5a). The E-cad immobile fraction comprised 59% of the total E-cad and the recovery time of a single bleached cluster was about 260 s (Fig. 7a and Supplementary Fig. 4b); this lies in the typical range for epithelial cells[28,34]. E-cad anchoring to the actin cortex proved essential for puncta organization and stability. Indeed, S180wt cell doublets expressing E-cad without a cytoplasmic domain (truncated at the transmembrane domain) exhibited scattered clusters over the contact area, with no accumulation at the rim (Fig. 1c); a similar distribution was observed on α-catenin knockdown (Fig. 1d and Supplementary Fig. 1d). In both cases, clusters were highly transient and mobile, confirming the ability of E-cad clusters to form in the absence of actin anchoring, in line with previous reports[25] and 2D simulations[24]. Our observations ruled out a passive convection of cadherin by a radial actin flow and demonstrated that puncta stability at the contact rim depends on actin anchoring.

To gain further insight into the concomitant reorganization of E-cad and actin, we followed the dynamics of junction formation in S180-E-cad–GFP cells. Junction expansion comprised three distinct steps, as illustrated by the time-lapse images in Fig. 1e and in Supplementary Video 3. Over the first 1–5 min after physical contact, the cells exhibited no detectable actin or E-cad reorganization. The cortex began to deplete at the contact zone concomitant with the scattered formation of E-cad puncta. Some puncta appeared directly at the edge whereas others migrated radially to finally accumulate at the rim. The actin depleted from the contact region but did not appreciably accumulate at the rim when compared to the rest of the cortex nor did it under E-cad clusters (Fig. 1f). The contacts attained their final size within typically 13 ± 6 min (s.d., $n = 26$). Individual puncta trajectories were followed by tracing the kymograph along the orthoradial coordinate of the contact rim (Fig. 2a). Remarkably, the number of clusters increased proportionally to the contact radius either by splitting or by intercalation events. Their average centre-to-centre distance thus remained constant at 1.4 ± 0.2 μm (s.d.) during the entire process (Fig. 2d). In established junctions, the cluster positions remained stable, whereas dim mobile clusters transiently appeared at the contact area. These changes resembled the recently observed differential properties of cadherins located either at the

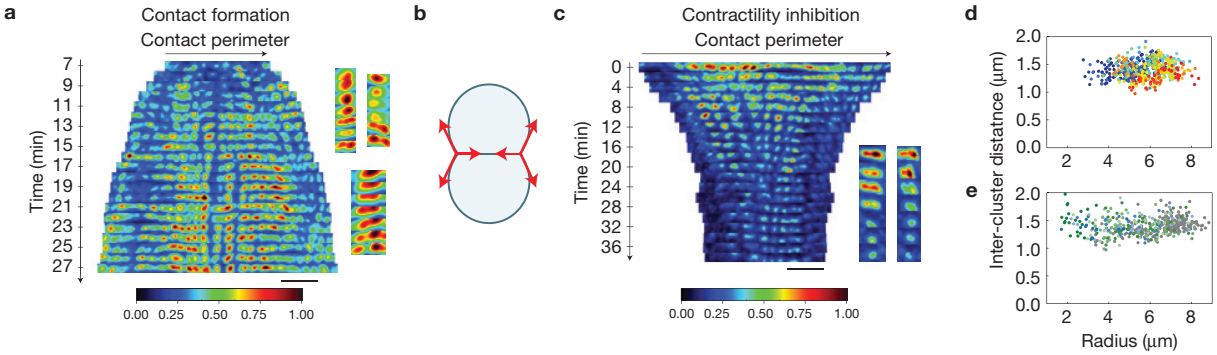

Figure 2 The contact is under tension. (**a**) Kymograph of the E-cad distribution along the contact perimeter during formation (scale bar 4 μm). Zoomed-in view of a punctum undergoing splitting (right). (**b**) Schematic of the force balance at the junction. (**c**) Kymograph of the E-cad distribution on contractility inhibition with Y27632 at 10 μM (scale bar 4 μm). Zoomed-in view of two puncta undergoing merging (right). (**d**) Inter-cluster distance as a function of the contact radius during formation, with a sampling rate $\Delta t = 2$ min, $n = 26$ kinetics of formation (colours correspond to individual formation) and a total of 585 time points. (**e**) Inter-cluster distance as a function of the contact radius at steady state in control conditions ($n = 214$ doublets, grey circles) and after contractility inhibition with Y27632 at 2 μM ($n = 49$ doublets, 5 μM ($n = 47$ doublets), 10 μM ($n = 44$ doublets) and 20 μM ($n = 23$ doublets) (green circles) and blebbistatin at 1 μM ($n = 22$ doublets), 5 μM ($n = 17$ doublets) and 50 μM ($n = 12$ doublets; blue circles).

apical or lateral regions of the epithelial junctions[22]. Monitoring the changes of the steady state of the stereotypical distribution of clusters enabled us to quantitatively evaluate E-cad recruitment under internal force variations.

Contractility favours contact expansion

Given the absence of extracellular matrix adhesion and the existence of a weak cortex on the junction area, we can assume that the forces borne by the cell–cell contact result solely from the tension generated by the cortical actin as described in Fig. 2b. The mean cortical tension measured by pipette aspiration was 900 pN μm^{-1} (Supplementary Fig. 5d). The total intercellular force exerted on the junction perimeter (44 μm on average) is thus 40 nN. This value falls into the low range of the integrated normal forces exerted at epithelial cell–cell junctions as inferred from the traction forces measured by traction force microscopy[35,36]. On contractility inhibition (Y27632 at 10 μM), the contact size shrank by 25% and the cortical tension reduced by twofold, consistent with previous reports[37]. We concluded that the contact region was under extension forces generated by myosin II. The inter-cluster distance remained constant at 1.4 ± 0.2 μm (s.d) independently of the inhibitor concentration (Fig. 2e). Cluster fusion during contact shrinking (Fig. 2c) maintained their constant linear density, mirroring the contact expansion. Interestingly, contact expansion was matched with an increase in the intensity of individual clusters, whereas contact shrinking in response to contractility inhibition led to a sharp decrease of E-cad recruitment. We then further characterized the quantitative relationship between E-cad recruitment and contractility.

Gradient of myosin II activity induces anisotropic recruitment of E-cad and E-cad partners

In control cells, the contact rim appeared brighter in some regions leading to an anisotropic distribution of E-cad (Fig. 3a). We examined whether these heterogeneities of E-cad density were related to variations in the local level of contractility. We thus correlated the local gradient of phosphorylated myosin with the anisotropy of the E-cad distribution. Anisotropy was measured by a vector **a** pointing from the centre of the contact to the centroid of the E-cad distribution along the ring. Myosin II activity was then mapped in doublets immunostained against the phosphorylated form of myosin light chain. The ring images were rescaled and reoriented ($n = 19$) along their E-cad anisotropy (Supplementary Fig. 2a,b). On average, we observed a twofold increase in E-cad intensity on the bright side as compared with the dim side (Fig. 4a,b). Ultimately, the asymmetric E-cad distribution seemed to be highly correlated with a gradient of pMLC (Fig. 4a,b). However, the myosin II gradient was not solely localized at the contact but extended vertically over a few micrometres. The localization of other junctional proteins tagged with RFP was also examined *in vivo*. The average static E-cad anisotropy was closely mirrored by the asymmetric distribution of α-catenin and p120 catenin, which merely localized at the contact rim. The myosin II gradient correlated with actin, myosin VI and EPLIN distributions, which extended along the cell cortex away from the contact. Vinculin was also present at the junction but its distribution exhibited no distinguishable asymmetry. The existence of an asymmetry in E-cad suggested the possibility, in this context, for an additional regulation mechanism to the ones already reported[27,38] that was not specifically associated with vinculin recruitment. We investigated the possibility of a non-local regulation mechanism of E-cad recruitment based on internal forces generated by myosin II.

The existence of a myosin II gradient led to dynamic spontaneous deformations of the doublets due to the imbalance of contractile stresses along the contact. These deformations occurred in bursts separated by quiescent periods around a preferential direction possibly imposed by the position of the doublet in the microwell. We measured deformation $\mathbf{d}_1$ (respectively, $\mathbf{d}_2$) to the top (respectively, bottom) cell relative to the contact area (Fig. 3b and Supplementary Fig. 2c–e). The overall deformation $\mathbf{d}=(\mathbf{d}_1+\mathbf{d}_2)/2$ (±64°) and the E-cad anisotropy vector **a** (±47°; Fig. 3c,d and Supplementary Fig. 2f) proved collinear and correlated over time. Our results set the upper limit of the dynamic time scale of E-cad recruitment below 8 s because no significant phase shift between the fluctuations of **d** and **a** could be detected. The causality between force generation and E-cad recruitment was further investigated.

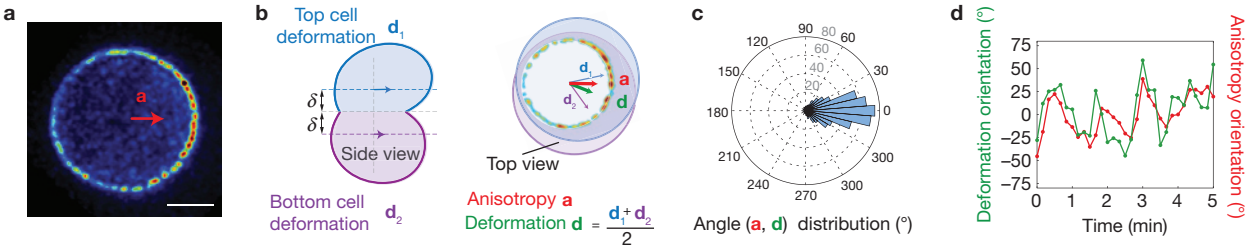

Figure 3 E-cad dynamic recruitment following spontaneous deformation. (**a**) Typical anisotropy for the distribution of the intensity of E-cad puncta (scale bar 5 μm). (**b**) Schematic doublet undergoing deformation. Side view with top and bottom cell deformation calculated on a slice taken 1.5 μm above and below the junction (left). Top view with mean deformation and anisotropy vectors (right). (**c**) Angle distribution between the mean deformation and the anisotropy vector taken during formation and at steady state ($n = 28$ doublets with a total of 572 time points). (**d**) Typical variation over time of the mean deformation and anisotropy orientation.

Modulation of actin turnover regulates E-cad immobilization

E-cad local accumulation proved concomitant with marked changes in E-cad dynamics. Using fluorescence recovery after photobleaching (FRAP), we simultaneously monitored the dynamics of individual clusters in the bright and dim region (Fig. 5a) once the junction had reached a steady state (reduced fluctuations). Kymographs of the recovery are shown in Fig. 5b and Supplementary Fig. 4a. The immobile fraction (IF; no recovery after 12 min) of cadherins is significantly higher in the bright regions (Fig. 5c). We estimated the pool of immobile cadherins (IP) per unit length as the immobile fraction times the normalized intensity of the region i_{reg} before bleaching: $IP = IF.\frac{i_{reg}}{\langle i \rangle_{ring}}$, where $\langle i \rangle_{ring}$ is the average intensity of the ring. Figure 5d clearly demonstrated the asymmetric distribution of the immobile pool whereas the mobile pool was uniformly distributed along the ring. We concluded that the local accumulation of cadherins in the bright region originated from a local immobilization of E-cad as demonstrated in Fig. 5c,d. Recovery times are shown in Supplementary Fig. 4d. The relative enrichment of the immobile pool, $\Delta IP/IP_{dim}$, scaled linearly with the relative intensity $\Delta i/i_{dim}$, namely

$$\Delta IP/IP_{dim} = 1.2\Delta i/i_{dim} \quad (1)$$

(Fig. 5e). As E-cad enrichment correlated with changes in E-cad dynamic properties, we reasoned that the immobilization stemmed from a change in the turnover rate of the underlying cortical actin. Indeed, the actin recovery after photobleaching (Fig. 5g) measured on S180-E-cad–GFP cells transfected with actin–RFP was asymmetric with longer times found in the E-cad bright regions (Fig. 5f,i). The actin mobile fraction in both regions was constant. The strong correlation between actin turnover and E-cad recruitment was uncovered by the proportionality between the degrees of anisotropy, as captured by the relative increment in intensity and the relative increment in actin recovery time, namely

$$\Delta i/i_{dim} = 1.7\Delta\tau/\tau_{dim} \quad (2)$$

(Fig. 5j). Using the relationship between equation (1) and equation (2), we found that $\Delta IP/IP_{dim} = 2.0 \pm 0.3\Delta\tau/\tau_{dim}$. Our data clearly demonstrate that E-cad immobilization is directly correlated with the modulation of actin dynamics. Taken together, these findings suggest that myosin II activity, actin dynamics and sequestration of E-cad in the adherent puncta are involved in a feedback loop.

Myosin II activity regulates E-cad immobilization by modulation of actin turnover

We then used drugs to modulate the global cell contractility and sought to determine the correlative changes in E-cad recruitment and in actin dynamics at the junction. Contractility inhibition using blebbistatin and Y27632 led to a decrease of the contact radius as well as a reduction in the concentration of E-cad in individual puncta in a concentration-dependent manner (Fig. 6a and Supplementary Fig. 5b). The reversibility of the process was further confirmed by subsequent drug removal, resulting in contact expansion and E-cad upregulation. Independent of drug treatment, we unveiled a clear correlation between the relative variation in the mean E-cad fluorescence along the ring $I_{drug}/I_{vehicle}$ versus that in the contact radius $R_{drug}/R_{vehicle}$ (Fig. 6b and Supplementary Fig. 5b). Reciprocally, under contractility stimulation by nocodazole[39], the contact enlarged and the E-cad recruitment was enhanced (Fig. 6a,b). In addition, systematic measurements of cortical tension by pipette aspiration for all drug treatment conditions were performed. The results demonstrated that contact size was directly correlated to cortical tension (Fig. 6c and Supplementary Fig. 5d).

We then tested whether E-cad recruitment resulted directly from changes in the level of the intercellular force or indirectly through the modulation of actin dynamics. Systematic FRAP measurements on E-cad and actin were performed after Y27632 treatment. The increase in E-cad recruitment with contractility was essentially accounted for by E-cad sequestration (Fig. 7a,b and Supplementary Fig. 4b). Correlatively, the actin turnover time was reduced with contractility (Fig. 7d), whereas the actin mobile fraction remained unchanged (Fig. 7c). As shown in Fig. 7e, the relative increment in the immobile pool on drug treatment IP_{drug} with respect to $IP_{vehicle}$ scaled linearly with the relative increment in actin turnover following drug treatment τ_{drug} with respect to $\tau_{vehicle}$; namely: $\Delta IP/IP_{vehicle} = 2.0 \pm 0.2\Delta\tau/\tau_{vehicle}$. This relationship is quantitatively similar to the one established along the myosin II gradient in control doublets. We concluded that myosin II contractility can regulate both the rate of actin turnover and E-cad recruitment.

To prove that actin turnover can regulate the level of E-cad recruitment independently of the application of a mechanical force at the junction, we directly altered actin dynamics using latrunculin (1 μM) and jasplakinolide (100 nM). In both cases, the cortical tension was reduced and led to shrinkage of the contact. However, the drugs created an antagonistic effect on the dynamic of actin. Latrunculin,

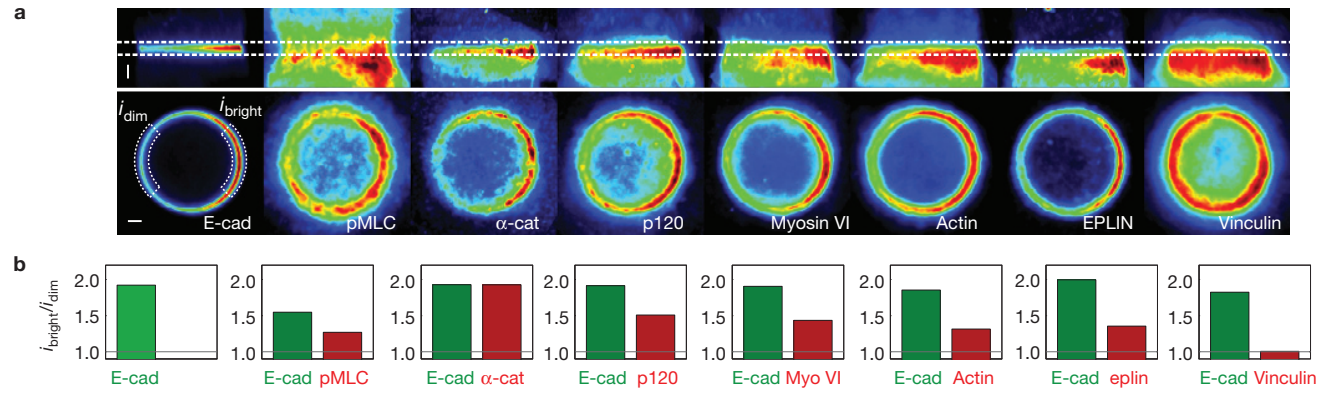

Figure 4 Mapping of E-cad key partners. (**a**) Average localization of E-cad (n= 142 doublets), phospho-MLC (n=19 doublets), α-catenin (n=7 doublets), p120 (n=10 doublets), myosin VI (n=18 doublets), actin (n=27 doublets), EPLIN (n=15 doublets) and vinculin (n=20 doublets) once superimposed after alignment along the E-cad anisotropy. Side view (top) and contact view (bottom; scale bar 2 μm). (**b**) Quantification of the anisotropy measured by the ratio of intensity between the bright side and dim side in the region surrounding the junction (as shown in **a**) for E-cad and key E-cad partners.

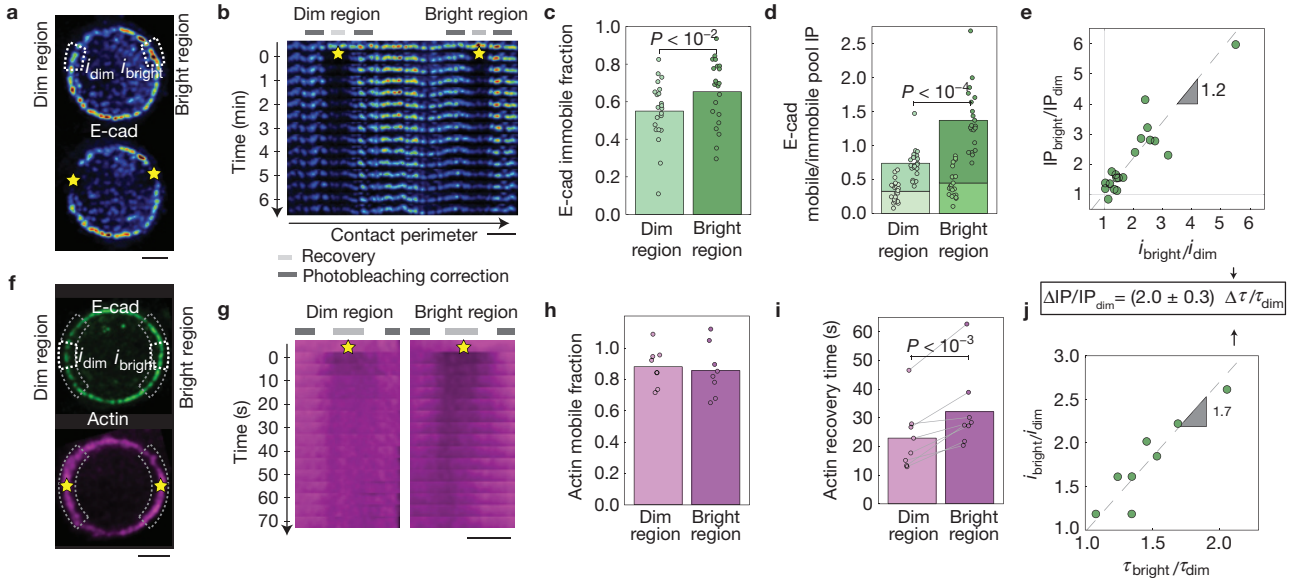

Figure 5 Comparative E-cad and actin dynamics on the same junction. (**a**) Localization of the two regions of interest (dim and bright) used to perform FRAP measurements on E-cad. (**b**) Typical kymograph of E-cad recovery after photobleaching. (**c**) E-cad immobile fraction in the dim and bright regions (n=22 doublets). (**d**) E-cad mobile (light) and immobile (dark) pools in the dim and bright regions (n=22 doublets). (**e**) Ratio of E-cad immobile pool between bright and dim regions versus ratio of E-cad intensity between bright and dim regions (n=22 doublets). (**f**) Localization of the two regions of interest (E-cad dim and bright sides) used to perform FRAP measurements on actin. (**g**) Typical kymographs of the actin recovery after photobleaching of the E-cad bright and dim regions. (**h**) Actin mobile fractions in the dim and bright regions (n=8 doublets). (**i**) Actin recovery time in the dim and bright region (n=8 doublets). (**j**) Ratio of E-cad intensity between bright and dim regions versus ratio of actin recovery time between bright and dim regions (n=8 doublets). **e**,**j** provides a relationship between the relative increment in the E-cad immobile pool and the relative increment in actin recovery time The P values in **c**, **d** and **i** are calculated from paired Student's t-tests. Scale bars, 5 μm.

preventing actin polymerization, increased actin turnover (Fig. 7d) and induced a marked downregulation of E-cad recruitment (Fig. 6b). In contrast, a low dose of jasplakinolide, stabilizing F-actin, decreased actin turnover (Fig. 7d) and increased E-cad recruitment (Fig. 6b). In both cases, recruitment variations stemmed from changes in the E-cad immobile pool (Fig. 7a,b). The actin mobile fraction remained fairly constant (Fig. 7c). We concluded that the modulation of actin dynamics can directly regulate the sequestration of E-cad at the junction (Fig. 7e). Overall, our data suggest that myosin II contractility is able to modulate actin turnover, which, in turn, regulates E-cad immobilization at adherens junctions.

DISCUSSION

Our data demonstrate a causal link between actin dynamics and E-cad recruitment. The slowdown of the actin turnover induces the increase of E-cad recruitment at the membrane. This effect is observed at the contacting and non-contacting membrane alike (Supplementary Fig. 5c). Changes in actin dynamics translate into the sequestration of E-cad exclusively at adhesion foci, probably due to stabilization by *trans*-dimerization. Furthermore, the local enrichment of E-cad in puncta of constant size as observed here (Supplementary Fig. 5a) biases the *trans*-dimerization equilibrium towards dimer formation, potentially providing a positive feedback loop towards sequestration.

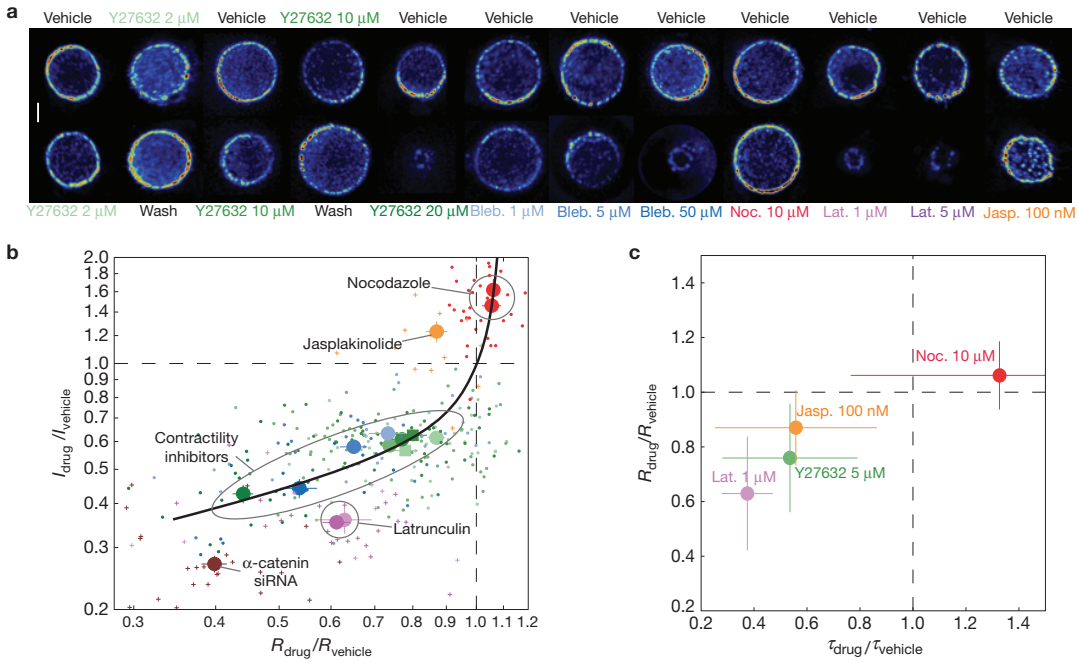

Figure 6 Myosin II activity and F-actin stability regulate the level of E-cad recruitment. (**a**) E-cad rings at steady state for different drug treatments. Doublets are formed in normal conditions (respectively in the presence of Y27632 at 2 μM ($n=25$ doublets) and 10 μM ($n=15$ doublets)) (top line) and subsequently treated with Y27632 at 2 μM ($n=24$ doublets), 5 μM ($n=24$ doublets), 10 μM ($n=29$ doublets) and 20 μM ($n=23$ doublets), blebbistatin at 1 μM ($n=22$ doublets), 5 μM ($n=17$ doublets) and 50 μM ($n=12$ doublets), nocodazole at 10 μM ($n=40$ doublets), latrunculin at 1 μM ($n=11$ doublets) and 5 μM ($n=22$ doublets) and jasplakinolide at 100 nM ($n=18$ doublets) (respectively washed) (bottom line; scale bar 5 μm). (**b**) Relative variation (between drug treatment and control conditions) in the average E-cad fluorescence versus relative variation in the contact radius. (**c**) Relative variation (between drug treatment and control conditions) in the contact radius of the doublets versus relative variation of cortical tension of single cells treated with latrunculin at 1 μM ($n=8$ doublets), Y27632 at 5 μM ($n=8$ doublets), jasplakinolide at 100 nM ($n=10$ doublets) and nocodazole at 10 μM ($n=9$ doublets). Error bars correspond to the standard deviation.

This result shed light on the possibility to use the dynamic properties of the actin cortex as a regulatory process to control the recruitment of cadherin at the membrane. Our conclusions are consistent with previous observations in which differential stabilization of F-actin at the apical and lateral regions of epithelial cell contacts leads to a gradient of cadherin diffusion properties along the lateral membranes in CaCo-2 cells[22]. Our results are also consistent with those in a previous study on *Drosophila*[33]. That study statistically inferred the dynamics of E-cad nanoscopic cluster fusion and fission from the changes in their size distribution. The mean junctional E-cad density measured in that study is compatible with ours (around 500 molecules per micrometre). The constant mobile pool we observed by FRAP in control experiments and on drug treatment echoes the constancy of monomer concentration for different junctional surface densities and drug treatments observed in ref. 33. In that study it was argued that the constancy of monomer concentration results from either strong binding in the *trans* configuration or an E-cad clustering that has a faster rate than the dissociation into monomers. We would add that if E-cad molecules within large clusters are immobilized (owing to a slower dynamics of the underlying cortical actin), they do not contribute in the exchange anymore, thus leading to an effective shift of the binding equilibrium. We observed that the regulation of the level of recruitment occurs by immobilizing E-cad molecules when the authors of ref. 33 see an enrichment in larger clusters in similar conditions. Assuming a slower turnover dynamics for larger clusters reconciles both observations, although we could not detect nanoscopic clusters with our observation method. For fast actin turnover (actin depolymerization), the E-cad density drops whereas for slow actin turnover (stabilization of F-actin), the E-cad density increases. The modulation of actin dynamic in *Drosophila* embryos leads to the shift of the mean junctional E-cad density in the same way as in our experiments.

We also demonstrated how the regulation of cadherin recruitment by actin dynamics participates in the mechanosensitive response of the adherens junction to intercellular forces. We propose that changes in myosin II contractility affect cortical actin turnover that in turn regulates E-cad recruitment. This mechanism corresponds to a mechanosensitive regulation of the adhesion strength and significantly differs from the present understanding of the mechanosensitive reinforcement of cell–cell adhesion based on the recruitment of additional actin at the junction. The best understood mechanisms for such recruitment are related to protein conformational changes such as those typical in α-catenin, which, on stretching, exposes a cryptic site for vinculin leading to subsequent actin binding[27]. It is then assumed that a higher concentration of actin would result in an enhanced recruitment of *trans*-membrane binders. The contractility-mediated actin turnover modulation that we have established is not exclusive of other well-established mechanosensitive mechanisms such as the one mentioned here and is expected to act in parallel or in a feedback loop.

With our approach, we could further decouple the role of tension and actin dynamics onto the E-cad recruitment. We showed that the direct modulation of the actin turnover dynamics can induce

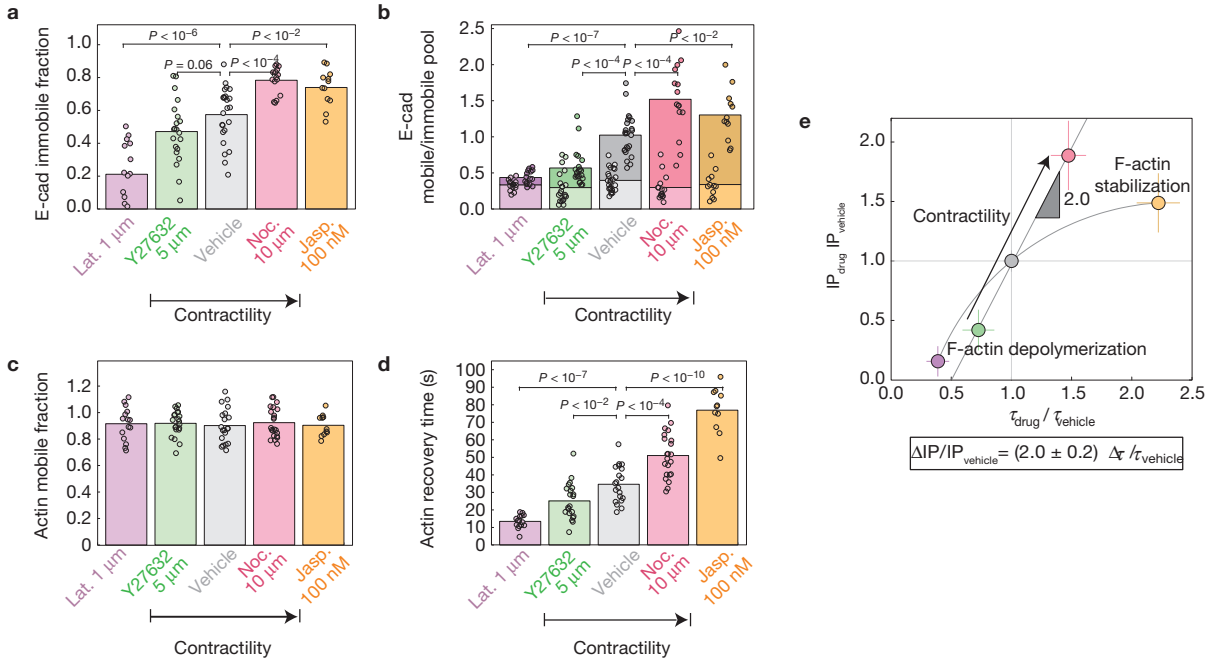

Figure 7 Comparative E-cad and actin dynamics following modulation of myosin II activity and F-actin stability. (**a**) E-cad immobile fraction for doublets treated with latrunculin at 1 µM ($n=15$ doublets), with Y27632 at 5 µM ($n=21$ doublets), in control conditions ($n=24$ doublets), with nocodazole at 10 µM ($n=15$ doublets) and with jasplakinolide at 100 nM ($n=12$ doublets). (**b**) E-cad mobile and immobile pools. (**c**) Actin mobile fraction for doublets treated with latrunculin at 1 µM ($n=15$ doublets), with Y27632 at 5 µM ($n=21$ doublets), in control conditions ($n=20$ doublets), with nocodazole at 10 µM ($n=22$ doublets) and with jasplakinolide at 100 nM ($n=11$ doublets). (**d**) Actin recovery time. (**e**) Ratio between E-cad immobile pool on drug treatment and E-cad immobile pool in control conditions versus ratio of actin recovery time following drug treatment and actin recovery time in control conditions for all drugs tested. The *P* values in **a**, **b** and **d** are calculated from unpaired Student's *t*-tests.

a large recruitment of E-cad at the junction by sequestration without a concomitant increase of the cortical tension (jaspakinolide treatment). Moreover we reported situations (ROCK inhibitor versus jasplakinolide treatment) where cell doublets exhibited equal cortical tension and similar contact size and yet showed significant variations of E-cad sequestration induced by different actin turnover. This observation is in line with the argument of refs 11,26 that demonstrated that the cohesive energy does not contribute to the force balance determining the contact size and should not be regarded as a driving force for contact extension. It suggests that the mechanosensitive regulation of adhesion, even though required to maintain the junction integrity and transmission of forces, does not influence the junction morphology in this context.

Last our data suggest that, in addition to the structural properties of actin (meshwork density, branching and spatial extension of bundles), the dynamic properties of the actin meshwork are also an important parameter to be considered to understand how forces are generated and transmitted by the cortical actin. Taken together, our results advocate for the importance of actin rheological properties in understanding the regulation and strength of cell–cell adhesion. □

METHODS

Methods and any associated references are available in the online version of the paper.

Note: Supplementary Information is available in the online version of the paper

ACKNOWLEDGEMENTS

This work was supported by MBI seed funding (NRF grant). V.V acknowledges additional support from the joint Singapore/France research laboratory LIA CAFS. J.P.T acknowledges IMCB A-star core funding.

AUTHOR CONTRIBUTIONS

W.E. performed the experiments and handled the data analysis. B.A. prepared the microwells. L.L.Y. prepared the plasmids. W.E., J.P.T. and V.V. conceived the experiments. W.E. and V.V. wrote the manuscript. V.V. supervised the work.

COMPETING FINANCIAL INTERESTS

The authors declare no competing financial interests.

Published online at www.nature.com/doifinder/10.1038/ncb2973
Reprints and permissions information is available online at www.nature.com/reprints

1. Kan, N. G. *et al.* Gene replacement reveals a specific role for E-cadherin in the formation of a functional trophectoderm. *Development* **134,** 31–41 (2007).
2. Gumbiner, B. A functional assay for proteins involved in establishing an epithelial occluding barrier: Identification of a uvomorulin-like polypeptide. *J. Cell Biol.* **102,** 457–468 (1986).
3. Takeichi, M. The cadherins: Cell-cell adhesion molecules controlling animal morphogenesis. *Development* **102,** 639–655 (1988).
4. Schmalhofer, O., Brabletz, S. & Brabletz, T. E-cadherin, beta-catenin, and ZEB1 in malignant progression of cancer. *Cancer Metastasis Rev.* **28,** 151–166 (2009).
5. Stepniak, E., Radice, G. L. & Vasioukhin, V. Adhesive and signaling functions of cadherins and catenins in vertebrate development. *Cold Spring Harb. Perspect. Biol.* **1,** a002949 (2009).
6. Huang, R. Y-J., Guilford, P. & Thiéry, J-P. Early events in cell adhesion and polarity during epithelial-mesenchymal transition. *J. Cell Sci.* **125,** 4417–4422 (2012).
7. De Beco, S., Amblard, F. & Coscoy, S. New insights into the regulation of E-cadherin distribution by endocytosis. *Inter. Rev. Cell Mol. Biol.* **295,** 63–108 (2012).
8. Lecuit, T. & Le Goff, L. Orchestrating size and shape during morphogenesis. *Nature* **450,** 189–192 (2007).
9. Lecuit, T., Lenne, P-F. & Munro, E. Force generation, transmission, and integration during cell and tissue morphogenesis. *Annu. Rev. Cell Dev. Biol.* **27,** 157–184 (2011).

10. Käfer, J., Hayashi, T., Marée, A. F. M., Carthew, R. W. & Graner, F. Cell adhesion and cortex contractility determine cell patterning in the *Drosophila* retina. *Proc. Natl Acad. Sci. USA* **104,** 18549–18554 (2007).
11. Manning, M. L., Foty, R. A., Steinberg, M. S. & Schoetz, E-M. Coaction of intercellular adhesion and cortical tension specifies tissue surface tension. *Proc. Natl Acad. Sci. USA* **107,** 12517–12522 (2010).
12. Shewan, A. M. Myosin 2 is a key rho kinase target necessary for the local concentration of E-cadherin at cell–cell contacts. *Mol. Biol. Cell* **16,** 4531–4542 (2005).
13. Miyake, Y. *et al.* Actomyosin tension is required for correct recruitment of adherens junction components and zonula occludens formation. *Exp. Cell Res.* **312,** 1637–1650 (2006).
14. Krendel, M. *et al.* Myosin-dependent contractile activity of the actin cytoskeleton modulates the spatial organization of cell–cell contacts in cultured epitheliocytes. *Proc. Natl Acad. Sci. USA* **96,** 9666–9670 (1999).
15. Taguchi, K., Ishiuchi, T. & Takeichi, M. Mechanosensitive EPLIN-dependent remodeling of adherens junctions regulates epithelial reshaping. *J. Cell Biol.* **194,** 643–656 (2011).
16. Rauzi, M., Lenne, P-F. & Lecuit, T. Planar polarized actomyosin contractile flows control epithelial junction remodelling. *Nature* **468,** 1110–1114 (2010).
17. Adams, C. L., Chen, Y. T., Smith, S. J. & James Nelson, W. Mechanisms of epithelial cell–cell adhesion and cell compaction revealed by high-resolution tracking of E-cadherin–green fluorescent protein. *J. Cell Biol.* **142,** 1105 (1998).
18. Vasioukhin, V., Bauer, C., Yin, M. & Fuchs, E. Directed actin polymerization is the driving force for epithelial cell–cell adhesion. *Cell* **100,** 209–219 (2000).
19. Ehrlich, J. S., Hansen, M. D. H. & Nelson, W. J. Spatio-temporal regulation of Rac1 localization and lamellipodia dynamics during epithelial cell–cell adhesion. *Dev. Cell* **3,** 259–270 (2002).
20. Yamada, S. & Nelson, W. J. Localized zones of Rho and Rac activities drive initiation and expansion of epithelial cell–cell adhesion. *J. Cell Biol.* **178,** 517–527 (2007).
21. Priya, R., Yap, A. S. & Gomez, G. A. E-cadherin supports steady-state Rho signaling at the epithelial zonula adherens. *Differentiation* **86,** 133–140 (2013).
22. Wu, S. K. *et al.* Cortical F-actin stabilization generates apical-lateral patterns of junctional contractility that integrate cells into epithelia. *Nat. Cell Biol.* **16,** 167–178 (2014).
23. Harrison, O. J. *et al.* The extracellular architecture of adherens junctions revealed by crystal structures of type i cadherins. *Structure* **19,** 244–256 (2011).
24. Wu, Y. *et al.* Cooperativity between trans and cis interactions in cadherin-mediated junction formation. *Proc. Natl Acad. Sci. USA* **107,** 17592–17597 (2010).
25. Hong, S., Troyanovsky, R. B. & Troyanovsky, S. M. Binding to F-actin guides cadherin cluster assembly, stability, and movement. *J. Cell Biol.* **201,** 131–143 (2013).
26. Maître, J-L. *et al.* Adhesion functions in cell sorting by mechanically coupling the cortices of adhering cells. *Science* **338,** 253–256 (2012).
27. Yonemura, S., Wada, Y., Watanabe, T., Nagafuchi, A. & Shibata, M. α-Catenin as a tension transducer that induces adherens junction development. *Nat. Cell Biol.* **12,** 1–22 (2010).
28. Cavey, M., Rauzi, M., Lenne, P-F. & Lecuit, T. A two-tiered mechanism for stabilization and immobilization of E-cadherin. *Nature* **453,** 751–756 (2008).
29. Ladoux, B. *et al.* Strength dependence of cadherin-mediated adhesions. *Biophys. J.* **98,** 534–542 (2010).
30. Tabdili, H. *et al.* Cadherin-dependent mechanotransduction depends on ligand identity but not affinity. *J. Cell Sci.* **125,** 4362–4371 (2012).
31. Dufour, S., Beauvais-Jouneau, A., Delouvée, A. & Thiery, J. P. Differential function of N-cadherin and cadherin-7 in the control of embryonic cell motility. *J. Cell Biol.* **146,** 501–516 (1999).
32. Chu, Y. S. Force measurements in E-cadherin-mediated cell doublets reveal rapid adhesion strengthened by actin cytoskeleton remodeling through Rac and Cdc42. *J. Cell Biol.* **167,** 1183–1194 (2004).
33. Truong Quang, B-A., Mani, M., Markova, O., Lecuit, T. & Lenne, P-F. Principles of E-cadherin supramolecular organization *in vivo*. *Curr. Biol.* **23,** 2197–2207 (2013).
34. De Beco, S., Gueudry, C., Amblard, F. & Coscoy, S. Endocytosis is required for E-cadherin redistribution at mature adherens junctions. *Proc. Natl Acad. Sci. USA* **106,** 7010–7015 (2009).
35. Maruthamuthu, V., Sabass, B., Schwarz, U. S. & Gardel, M. L. Cell–ECM traction force modulates endogenous tension at cell–cell contacts. *Proc. Natl Acad. Sci. USA* **108,** 4708–4713 (2011).
36. Liu, Z. *et al.* Mechanical tugging force regulates the size of cell–cell junctions. *Proc. Natl Acad. Sci. USA* **107,** 9944–9949 (2010).
37. Tinevez, J-Y. *et al.* Role of cortical tension in bleb growth. *Proc. Natl Acad. Sci. USA* **106,** 18581–18586 (2009).
38. Maddugoda, M. P., Crampton, M. S., Shewan, A. M. & Yap, A. S. Myosin VI and vinculin cooperate during the morphogenesis of cadherin cell cell contacts in mammalian epithelial cells. *J. Cell Biol.* **178,** 529–540 (2007).
39. Chang, Y-C., Nalbant, P., Birkenfeld, J., Chang, Z-F. & Bokoch, G. M. GEF-H1 couples nocodazole-induced microtubule disassembly to cell contractility via RhoA. *Mol. Biol. Cell* **19,** 2147–2153 (2008).

DOI: 10.1038/ncb2973

METHODS

Antibodies and plasmids. The anti-phospho-myosin light chain 2 antibody (#3671), which targets the phosphorylated serine residue at position 19, was purchased from Cell Signaling Technology and used at a 1:50 dilution. All RFP Gateway system vectors and EPLIN were purchased from Invitrogen.

siRNA against α-catenin was purchased from Dharmacon (on Targetplus SMARTpool siRNA, Ctnna1, Cat No: L-048960-01) and targeted against the sequence 5′-UGUAGAAGAUGUUCGAAAA-3′.

All protein plasmids (α-catenin, p120 catenin, myosin VI, actin, vinculin, EPLIN) were cloned into the Gateway acceptor plasmid (Invitrogen) and recombined with the RFP donor plasmid from the Gateway system. Sequencing was performed to ensure proper insertion.

Cell culture and transfection. S180 cells[32,36] stably transfected with E-cad–GFP were provided by J. P.T. and tested for mycoplasma. S180 cells were cultured in high-glucose DMEM, supplemented with 10% FBS. Cells at 80% confluence were detached by flushing medium over the Petri dish to obtain a single-cell suspension. A glass-bottom dish with microwells was mounted onto the microscope stage and immersed in CO_2-independent medium supplemented with 10% FBS. Cell seeding was achieved by adding one drop of this single-cell suspension. Cells were transfected using Lipofectamine 2000 (Invitrogen) for the expression of plasmids.

Microwell preparation. A master mould with an array of 20-μm-diameter holes was fabricated in SU8-3050 resist on a silicon wafer using standard lithography techniques. The thickness of the SU8 layer sets the height of the microwells (here, 50 μm). The master mould was then silanized for 2 h under vacuum with trichloro (1H,1H,2H,2H-perfluorooctyl) silane (Sigma-Aldrich). Polydimethylsiloxane (PDMS) was cast onto the mould and cured for 2 h at 80 °C to obtain the negative of the master mould. Once detached, the PDMS stamp was cut into 5× 5-mm pieces. A piece was then gently laid directly on the coverslip of a glass-bottom dish (Iwaki). A drop of an ultraviolet-curable polymer MY134 DC (My Polymers) was deposited on one edge, which filled the gap between the substrate and the stamp by capillarity. After curing, the PDMS stamp was removed. Finally, the polymer was treated with Pluronic acid (Sigma-Aldrich) to achieve antifouling of the microwells.

Live-cell microscopy. Images were acquired using a spinning-disc confocal system (CSU-X Yokogawa) mounted on an inverted microscope (Eclipse Ti, Nikon Instruments) with an EMCCD camera Evolve 512 (Photometrics) and a Plan Apo ×100/1.4 NA oil immersion objective (Nikon). Time-lapse and still images were taken as 10–40 z-stacks in 0.5-μm z-steps). Two laser lines were used at 491 nm and 561 nm (50 mW, Cobolt).

Imaging cell–cell contact of suspended doublets. As doublets are constantly wriggling, cell–cell contact always presents at a certain inclination. Therefore, we imaged a 5–10-μm-thick volume that circumscribed the contact. The stacks were then processed to observe the contact in a fixed frame of reference. The image processing essentially consisted of deconvoluting each stack and interpolating it onto a grid plane (P_0) that cuts through the ring. P_0 is defined by two angles, θ_1 and θ_2, for the inclination and the 3D coordinates of the centre of the contact (x_0, y_0, z_0) (Supplementary Fig. 1a). A Matlab code was developed to determine automatically these five parameters. To determine θ_1, the stack was rotated along the z axis and projected along the y direction to obtain the side view. The side view was thresholded by keeping 1% of the brightest pixels and integrated. θ_1 is the angle for which the integration is minimal and corresponds to the flattening of the ellipse into a line segment. For θ_2, we interpolated the side view along different lines of different orientations that are integrated. θ_2 is given by the line passing through the ring for which the integration is maximal. The stack was then re-orientated so that the contact was horizontal. In this frame of reference, z_0 was given by the slice for which the image integration was maximal. x_0 and y_0 were obtained by fitting the ring, which also provided the contact radius. (x_0, y_0, z_0) were finally expressed in the initial frame of reference. As some clusters may be slightly out of P_0, the stack was interpolated on a series of grid planes parallel to P_0 covering a thickness range of ±1 μm with respect to P_0, thus defining a new 3D stack. The z-step between two consecutive planes, as well as the grid pitch, was taken equal to the pixel resolution. Contact imaging was finally achieved by projecting this stack along the z axis. For consistency, all quantitative measurements were performed on stacks imaged at ×100 magnification with the same camera (pixel size 160 nm). The contact was now observed in a fixed frame of reference located on the centre of the ring. Nevertheless, the doublet may rotate along its axis of revolution. To correct for these rotations, two consecutive images were registered using built-in Matlab algorithms or through manual correction (Supplementary Fig. 1b).

Measure of the spontaneous doublet deformation. To determine the dominant mode of deformation, the doublet was reoriented so that the contact was horizontal. In this frame of reference, we considered two slices (1.5 μm below and above the junction plane) and fitted the contour of the cell by a circle to finely determine the associated centre (x_1,y_1). If the doublet had a perfect symmetry of revolution (corresponding to a stress homogeneously distributed along the rim of the contact), this point would be on the axis of the revolution that cuts through the centre of the contact (x_0,y_0). Therefore, the deviation from this axis (x_1- x_0,y_1-y_0) measures the magnitude of the deformation (Supplementary Fig. 2c,d). Ultimately, the overall doublet deformation was simply obtained by averaging the bottom and top cell deformations (Supplementary Fig. 2d,e).

Optical aberration. By construction, optical aberrations were minimized by the almost-horizontal position of the junction. In addition, we checked for residual artefacts that could lead to the observed anisotropy and fluctuations. We first ruled out the potentiality of an anisotropy originating from differences in z positions along the rim of the contact. The E-cad ring always presented a region of enhanced recruitment spanning half the perimeter. As the amount of collected light decreased as the distance to the coverslip increased, it may be reasoned that the anisotropy resulted from an optical artefact due to the contact inclination. To test this hypothesis, we systematically determined for all our data whether the region of enhanced recruitment corresponded to the closest region of the coverslip. We did not see such a correlation, confirming that the anisotropy was not an optical artefact. Finally, the effect of stretching or compaction of the clusters in the z direction was tested. Reconstructed side views, as well as doublets imaged horizontally (tilted by 90°), did not show any significant deformations of the clusters. In addition, using a maximum intensity projection representation, we minimized the effect of the apparent z deformation due to the point spread function shape.

Fluorescent recovery after photobleaching. Mobile fractions and recovery times, τ, were determined by fitting the following exponential to the experimental recovery curves:

$$I(t) - I(0) = (I_\infty - I(0))(1 - e^{-t/\tau})$$

For FRAP measurements on untreated doublets, two regions of interest were bleached: the first on the bright side of the E-cad ring; the second, on the dim side. For FRAP measurements following drug treatment, these two regions were averaged to obtain the global response for the whole junction.

Cortical tension measurement. Single cells were deposited on a PEG-coated, glass-bottom dish. Micropipettes were pulled with a flaming pipette-puller (P-2000, Sutter Instruments), forged and bent to a 45° angle with a home-built forge. Pipettes were 7 μm in diameter. Before each measurement, the pressure in the pipette was equilibrated with the pressure in the dish. A detached cell was aspirated into the pipette with a low pressure. The pressure was then gradually decreased until the threshold pressure was reached, at which the cell formed a hemispherical protrusion in the pipette. The tension was computed using the Laplace law $\Delta P = 2T(1/r_P - 1/r_c)$, where r_c is the radius of the cell and r_P the radius of the pipette.

Repeatability of the experiments. Our results stem from the statistical analysis of multiple individual doublets. Doublets were formed between cells in culture with cell with passage numbers ranging 7 to 15 times. Each measurement constitutes an independent experiment because all of our experiments consist of comparing different parts of the cells or the same cell before and after drug treatment. Duplicates of experiments were also performed on at least 2 different days and typically 6 different days. The distributions of all data are shown.

Typical images represent series of experiments detailed as follows. Figure 1b: 25 cells over 2 different days; Fig. 1c: 12 doublets over 2 different days; Fig. 1d: 36 doublets over 2 different days; Fig. 1f: 25 cells over 2 different days; Fig. 2a: 26 doublets over 10 different days; Fig. 2c: 26 doublets over 3 different days; Fig. 4a: E-cad ($n = 142$ doublets), phospho-MLC ($n = 19$ doublets), α -catenin ($n = 7$ doublets), p120 ($n = 10$ doublets), myosin VI ($n = 18$ doublets), actin ($n = 27$ doublets), EPLIN ($n = 15$ doublets) and vinculin ($n = 20$ doublets) over 10 days; Fig. 5a,b: 22 doublets over 3 different days; Fig. 5f,g: 8 doublets over 3 different days; Fig. 6a: Y27632 at 2 μM ($n = 24$ doublets), 5 μM ($n = 24$ doublets), 10 μ M ($n = 29$ doublets) and 20 μM ($n = 23$ doublets), blebbistatin at 1 μM ($n = 22$ doublets), 5 μM ($n = 17$ doublets) and 50 μM ($n = 12$ doublets), nocodazole at 10 μ M ($n = 40$ doublets), latrunculin at 1 μM ($n = 11$ doublets) and 5 μM ($n = 22$ doublets) and jasplakinolide at 100 nM ($n = 18$ doublets) over 15 different days; Supplementary Fig. 1-c: MDCK-E-cad–GFP doublet ($n = 24$ cell doublets over 4 days) (left) and an embryonic stem cell E-cad–GFP doublet ($n = 26$ cells over 3 days) (right); Supplementary Fig. 3: E-cad ($n = 142$ doublets), phospho-MLC ($n = 19$ doublets), α-catenin ($n = 7$ doublets), p120 ($n = 10$ doublets), myosin VI ($n = 18$ doublets), actin ($n = 27$ doublets), EPLIN ($n = 15$ doublets) and vinculin ($n = 20$ doublets), over 10 different days.

DOI: 10.1038/ncb2973

nature cell biology

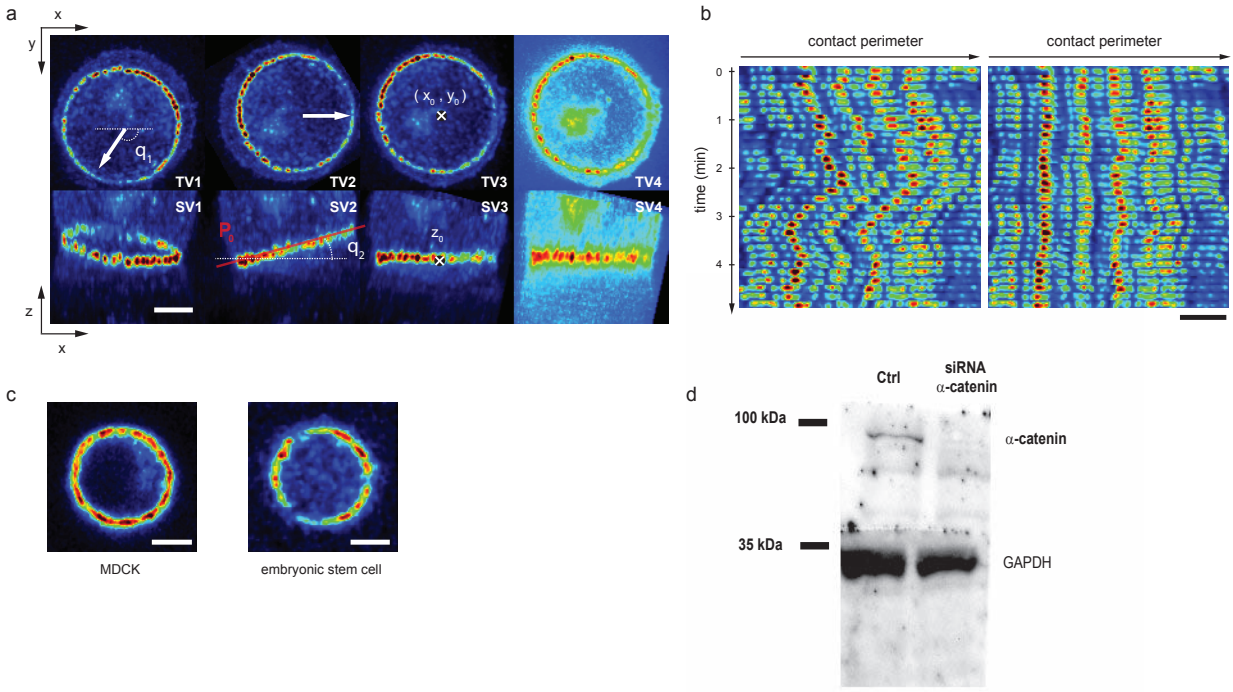

Supplementary Figure 1 Digital procedure for rotation compensation and comparison of E-cadherin junctional distribution for different cell types. **a.** Top view (TV1-4) and side view (SV1-4) of a 3D stack used for determining the coordinates of the contact plane. TV1-SV1: deconvoluted stack as imaged in confocal microscopy. TV2-SV2: deconvoluted stack after rotation along the z-axis. TV3-SV3: deconvoluted stack in the referential of the contact. TV4-SV4: raw data in the referential of the contact (scale bar 5 µm). **b.** Kymograph of a portion of the E-cad ring before and after image registration (scale bar 5 µm). **c.** Typical ring of a MDCK-E-cad–GFP doublet (n=24 cell doublets, 4 days) (left) and an embryonic stem cell E-cad–GFP doublet (n=26 cells , 3 days) (right) (scale bar 5 µm). **d.** Western blot of alpha catenin for control S180 cells and cells after alpha catenin knockdown. Cells used to look at the doublets had all the known phenotype of alpha catenin knockdown junctions displaying transient and dynamic cadherin clusters.

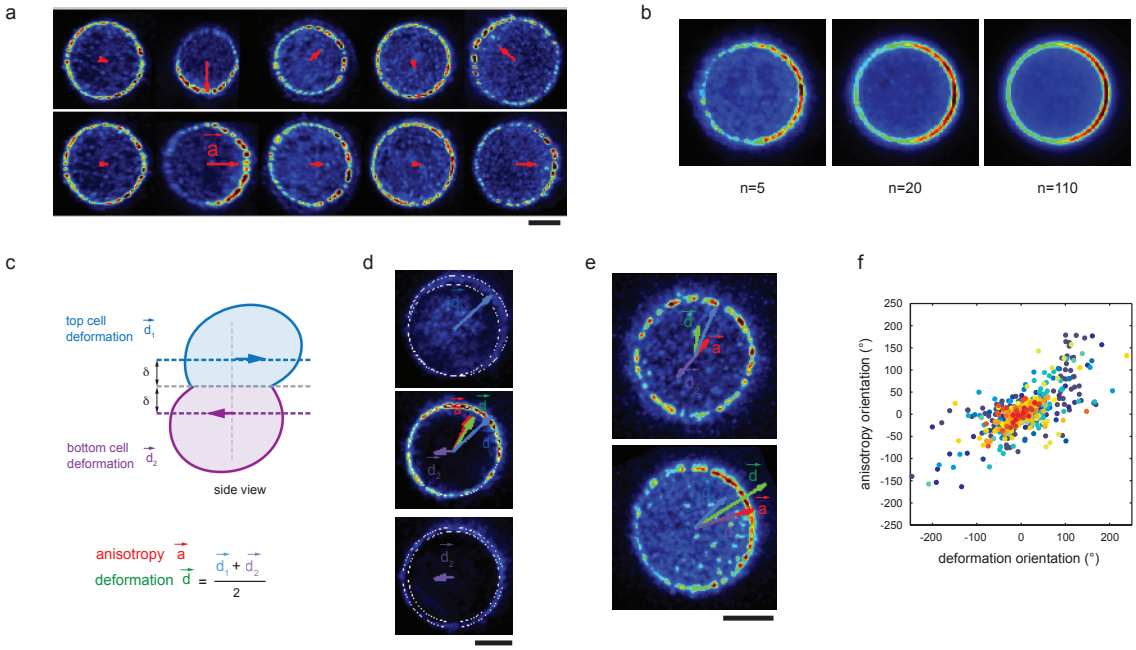

Supplementary Figure S2 Measurements of doublet deformation. **a.** Five rings and their anisotropy vector (top line). Same rings after rescaling and alignment of the anisotropy (bottom line) (scale bar 5 µm). **b.** Superimposition of n=5, 20 and 110 rings after image processing taken. **c.** Side view schematic of the doublet deformation. **d.** Images of the 2 slices taken 1.5 µm above and below the contact used to determine the contour of the cell (top and bottom). Image of the junction with anisotropy and deformation vectors (middle) (scale bar 5 µm). **e.** Extreme cases where d_1 and d_2 have opposite directions (isotrope ring) and same direction (anisotrope ring) (scale bar 5 µm). **f.** Anisotropy orientation as a function of the deformation orientation taken during contact formation and at steady state (n=28 doublets with a total number of 572 time-points).

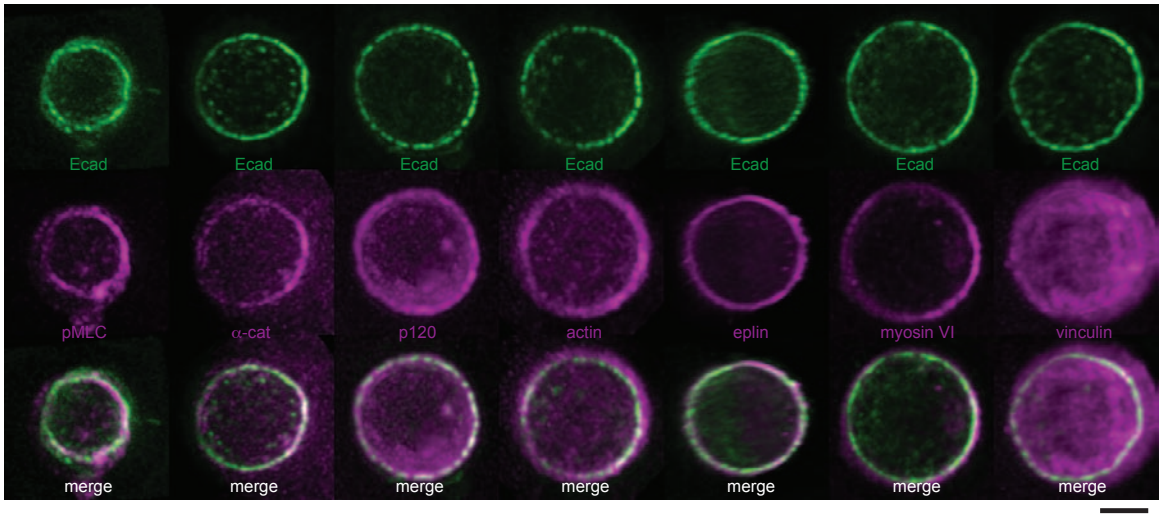

Supplementary Figure 3 Typical distribution of different junctional proteins. Typical distributions at the junction of E-cad, phospho-MLC, α-catenin, p120, actin, EPLIN, myosin VI and vinculin. The S180-Ecad-GFP cells were transfected with different junctional proteins tagged with m-cherry. The distribution of these proteins are compared to that of E-cad. A total of 116 doublets were observed (scale bar 5 μm).

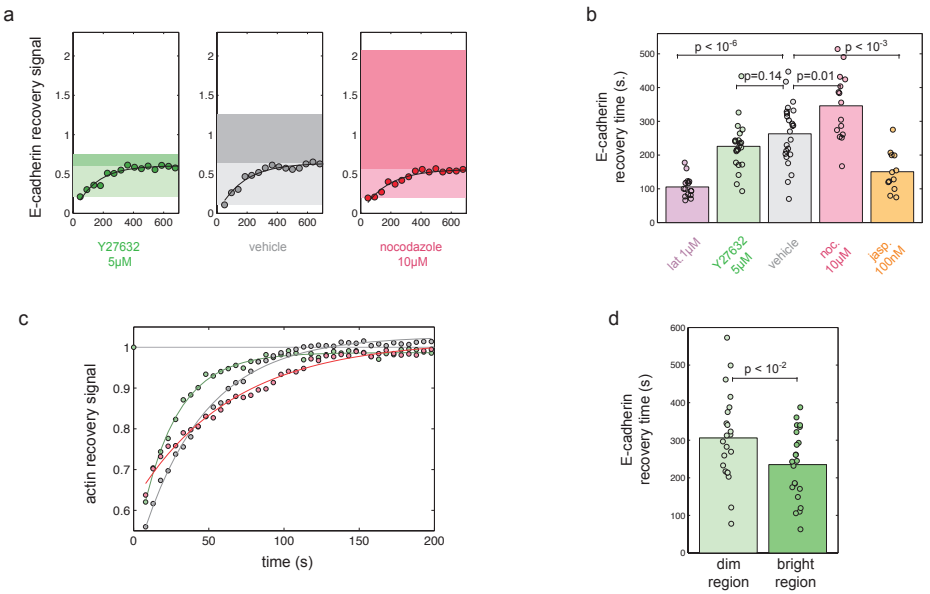

Supplementary Figure 4 FRAP measurements on E-cadherins and actin. **a.** Typical E-cad FRAP signal for a doublet treated with Y27632 at 5 μM, in control conditions and treated with nocodazole at 10 μM. **b.** E-cad recovery time for doublets treated with latrunculin at 1 μM (n=15 doublets), with Y27632 at 5 μM (n=21 doublets), in control conditions (n=24 doublets), with nocodazole at 10 μM (n=15 doublets) and with jasplakinolide at 100 nM (n=12 doublets). The p-values are calculated from unpaired Student's t-tests. **c.** Typical actin FRAP signal for a doublet treated with Y27632 at 5 μM, in control conditions and treated with nocodazole at 10 μM. **d.** E-cad recovery time in the dim region and the bright region of the same doublet (n=22 doublets). The p-value is calculated from a paired Student's t-test.

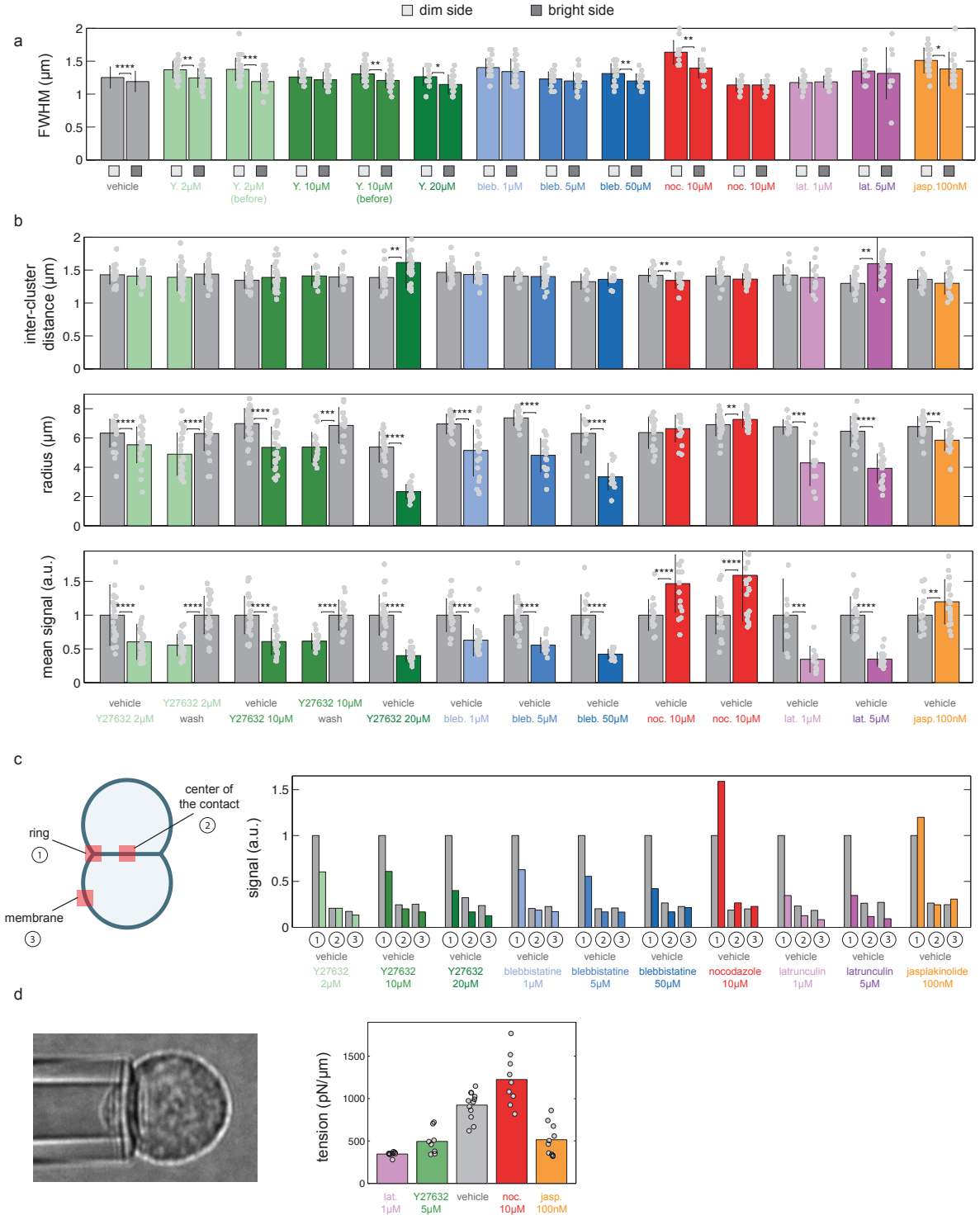

Supplementary Figure 5 Features of the E-cadherin distribution at the junction and cortical tension of single cells. Data in graphs **a-c** correspond to the same drugs and concentrations: Y27632 at 2 µM (n=49 doublets), 5 µM (n=24 doublets), 10 µM (n=44 doublets) and 20 µM (n=23 doublets); blebbistatin at 1 µM (n=22 doublets), 5 µM (n=17 doublets) and 50 µM (n=12 doublets); nocodazole at 10 µM (n=40 doublets); latrunculin at 1 µM (n=11 doublets), and 5 µM (n=22 doublets) and jasplakinolide at 100 nM (n=18 doublets) (*, p <0.05, **, p<0.01,***, p<0.001 ,****, $p<10^{-4}$). p-values are calculated from paired Student's t-test. The whole distributions of the data values are also shown. **a.** Average full-width at half maximum (FWHM) of the E-cad puncta on the dim side and on the bright side in control conditions (grey) and upon drug treatment. The error bars represent the standard deviation. The whole distribution is also shown. **b.** Inter-cluster distance, contact radius and mean E-cadherin signal along the ring in control conditions (grey) and upon drug treatment. The same statistical tests as **a.** were applied. **c.** E-cadherin density on the ring, at the center of the contact and on the membrane (as depicted in the schematic) in control conditions (grey) and upon drug treatment . **d.** Image of a single cell deformed by negative pressure (left). Cortical tension of single cells for different drug treatment: latrunculin 1 µM (n=8 doublets), Y27632 5 µM (n=8 doublets), control (n=12 doublets), nocodazole 10 µM (n=9 doublets) and jasplakinolide at 100 nM (n=10 doublets) (right).

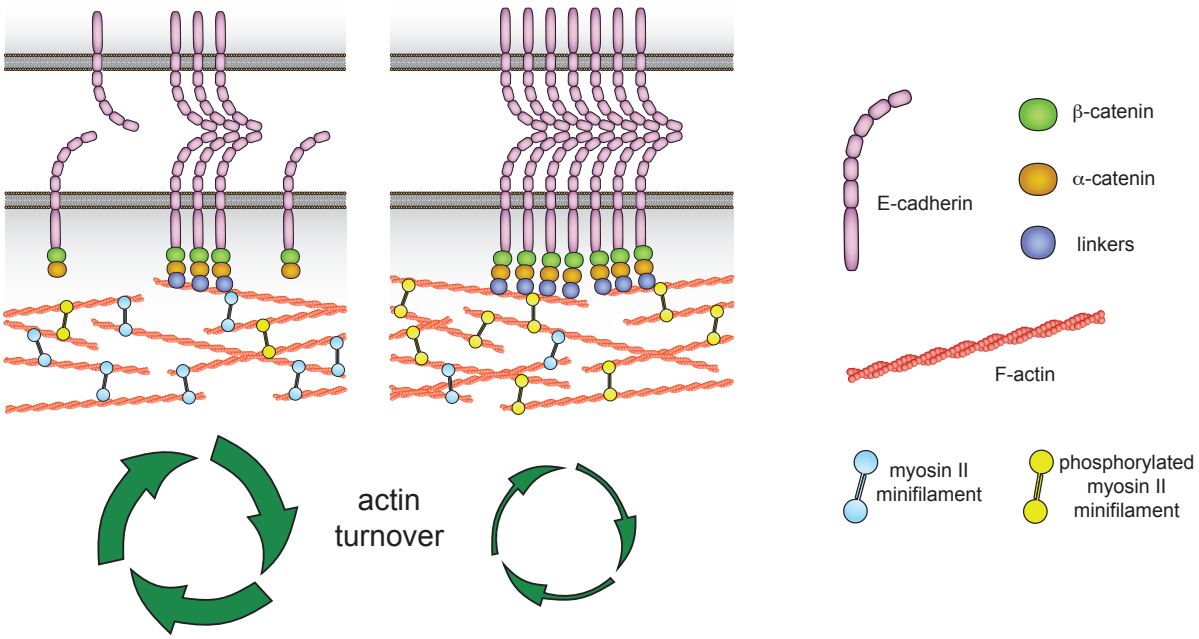

Supplementary Figure 6 Model of E-cadherin immobilization by actin turnover. We propose that the immobilization of E-cadherin is regulated by the turnover dynamics of the underlying actin cortex. In turn the turnover dynamics is modulated by the tension of the cortex generated by the actomyosin contractility. This mechanism provides a regulatory pathway for enhanced adhesion in cortex under tension.

Supplementary Video Legends

Supplementary video 1: Digital correction of residual rotations. Illustration of the different stages of correction for the residual rotations of the doublets. The doublets are imaged by confocal imaging with z-stacks spaced by 0.5 µm during the expansion of the contact (E-cad labeled with GFP). The movie displays the maximum intensity projection. From left to right: raw image, correction for azimuthal rotation, additional correction for rotation in the plane of the junction.

Supplementary video 2: Protocol for digital correction during contact expansion. Illustration of the effect of correction (see Movie 1) projected along the ZY plane.

Supplementary video 3: Dynamics of contact formation. Simultaneous dynamics of E-cad (green) and actin (magenta) localization at the rim of the contact during the contact expansion. Time t=0 corresponds to the initial physical contact between both cells.

Supplementary video 4: Cell contact shrinkage upon myosin II inhibition. Dynamics of the shrinkage of the contact after inhibition of myosin II activity by Y27632 at 10 µM. (Ecad GFP).

Supplementary video 5 Time correlation of cadherin anisotropy and doublet deformation. Correlated time variations of the E-cad distribution anisotropy a (red) and the doublet deformation at the level of the contact d (green).